

TA7  
W34c  
no.  
SL-92-4

c.3 US Army Corps  
of Engineers

CONTRACT REPORT SL-92-4

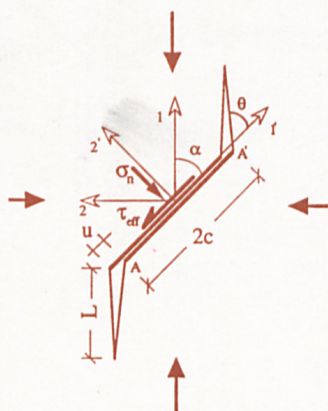
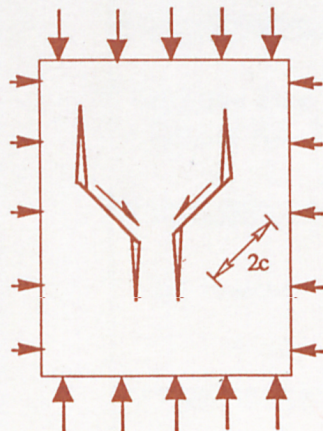
# CONSTITUTIVE MODELING OF ROCKS WITH INTERNAL CRACKS

by

Dusan Krajcinovic, Michal Basista

Mechanical and Aerospace Engineering  
Arizona State University  
Tempe, Arizona 85287-6106

US-CE-C PROPERTY OF THE  
UNITED STATES GOVERNMENT



April 1992

Final Report

Approved For Public Release; Distribution Is Unlimited

RESEARCH LIBRARY  
US ARMY ENGINEER WATERWAYS  
EXPERIMENT STATION  
VICKSBURG, MISSISSIPPI

Prepared for Defense Nuclear Agency  
6801 Telegraph Road, Alexandria, Virginia 22310-3398

Under Task Code RSRB, Work Unit 00272 (Task 4)  
Contract No. DACA39-91-M-2332

Monitored by Structures Laboratory  
US Army Engineer Waterways Experiment Station  
3909 Halls Ferry Road, Vicksburg, Mississippi 39180-6199





REPORT DOCUMENTATION PAGE			Form Approved OMB No. 0704-0188	
Public reporting burden for this collection of information is estimated to average 1 hour per response, including the time for reviewing instructions, searching existing data sources, gathering and maintaining the data needed, and completing and reviewing the collection of information. Send comments regarding this burden estimate or any other aspect of this collection of information, including suggestions for reducing this burden, to Washington Headquarters Services, Directorate for Information Operations and Reports, 1215 Jefferson Davis Highway, Suite 1204, Arlington, VA 22202-4302, and to the Office of Management and Budget, Paperwork Reduction Project (0704-0188), Washington, DC 20503.				
1. AGENCY USE ONLY (Leave blank)		2. REPORT DATE April 1992		3. REPORT TYPE AND DATES COVERED Final Report
4. TITLE AND SUBTITLE Constitutive Modeling of Rocks with Internal Cracks			5. FUNDING NUMBERS Contract No. DACA39-91-M-2332 Task Code RSRB Work Unit 00272	
6. AUTHOR(S) Dusan Krajcinovic, Michal Basista				
7. PERFORMING ORGANIZATION NAME(S) AND ADDRESS(ES) Arizona State University Tempe, AZ 85287-6106			8. PERFORMING ORGANIZATION REPORT NUMBER	
9. SPONSORING/MONITORING AGENCY NAME(S) AND ADDRESS(ES) See reverse.			10. SPONSORING/MONITORING AGENCY REPORT NUMBER Contract Report SL-92-4	
11. SUPPLEMENTARY NOTES Available from National Technical Information Service, 5285 Port Royal Road, Springfield, VA 22161.				
12a. DISTRIBUTION/AVAILABILITY STATEMENT Approved for public release; distribution unlimited.			12b. DISTRIBUTION CODE	
13. ABSTRACT (Maximum 200 words)  The analytical model discussed and formulated in this report focuses on the derivation of a constitutive model for low-porosity, crystalline rocks subjected to compressive stresses. The proposed model is inspired by micromechanical analyses of the kinked-crack mechanism. The report also discusses advantages and limitations of the proposed model listing topics requiring further research.  An illustrative example indicates that the suggested methodology leads to a relatively simple and tractable model which was, nevertheless, able to replicate major trends in the deformation process of a Westerly granite specimen in uniaxial compression. All major material parameters in the proposed analytical model are physically identifiable and experimentally measurable.				
14. SUBJECT TERMS Brittle response Granite Kinked crack			15. NUMBER OF PAGES 48	
			16. PRICE CODE	
17. SECURITY CLASSIFICATION OF REPORT UNCLASSIFIED			18. SECURITY CLASSIFICATION OF THIS PAGE UNCLASSIFIED	
19. SECURITY CLASSIFICATION OF ABSTRACT			20. LIMITATION OF ABSTRACT	

**9. (Continued).**

**Defense Nuclear Agency  
6801 Telegraph Road  
Alexandria, VA 22310-3398**

**USAE Waterways Experiment Station  
Structures Laboratory  
3909 Halls Ferry Road  
Vicksburg, MS 39180-6199**

## PREFACE

The investigation reported herein was conducted by Arizona State University (ASU) under Contract No. DACA39-91-M-2332 for the US Army Engineer Waterways Experiment Station (WES). The research was sponsored by the Defense Nuclear Agency (DNA) under Task Code RSRB, Work Unit 00272 (Task 4), "Damage Mechanics and Wave Propagation." The research was performed during the period of March 1991 to September 1991. The DNA work unit manager is Dr. Edward Tremba of the Weapons Effects Division, Shock Physics Directorate.

The principal investigator at ASU was Professor Dusan Krajcinovic. The report was written by Professor Krajcinovic and Dr. Michal Basista. The work was technically monitored by Drs. Behzad Rohani and Joseph S. Zelasko of the Geomechanics, Structures Laboratory (SL), WES. Mr. Bryant Mather is Director, SL.

At the time of publication of this report, Director of WES was Dr. Robert W. Whalin. Commander and Deputy Director was COL Leonard G. Hassell, EN.



## CONTENTS

Section	Page
Preface	i
Conversion Factors, Non-SI to SI (Metric Units) of Measurement	iii
1.0 Introduction	1
2.0 Mechanisms of Compression-Induced Microcracking in Rocks	3
3.0 Micromechanical Basis for a Phenomenological Damage Model	7
3.1 Deformation Process	8
3.2 Strain - Displacement Relations	15
3.3 Stress - Displacements Relationship	17
4.0 Phenomenological Model	21
4.1 Nondilatant Frictional Sliding	21
4.2 Microcracking	24
5.0 Illustrative Example	31
6.0 Remarks on the Brittle-to-Ductile Transition	35
7.0 Summary and Conclusions	36
8.0 References	38

## CONVERSION FACTORS, NON-SI TO SI (METRIC) UNITS OF MEASUREMENT

Non-SI units of measurements used in this report can be converted to SI (metric) units as follows:

<u>Multiply</u>	<u>By</u>	<u>To Obtain</u>
degrees (angle)	0.01745329	radians

# **CONSTITUTIVE MODELING OF ROCKS WITH INTERNAL CRACKS**

## **1.0 INTRODUCTION**

The objective of this short study is to examine possible avenues of formulating a practical phenomenological model for analyses of the deformation of rocks subjected to mechanical compressive stresses. In view of this objective a compelling argument can be made for simplicity as a necessary attribute of models suitable for large scale computations. A model of this type should emphasize salient aspects of the deformation process at the expense of unimportant details. For this reason micromechanical studies provide a necessary background for constitutive studies of actual engineering materials. Finally, the analytical studies discussed in this report will eventually become a part of a comprehensive package including necessary experimental verifications. It is, therefore, necessary to keep the number of material parameters at a minimum and identify these material parameters with underlying physical processes.

In order to further focus attention on mechanical response, only the quasi-static loading of dry rock specimens in isothermal conditions was considered in this initial phase of the work. The initial phase of this research program is restricted to studies of two-dimensional deformation problems of rock specimens subjected to large uniaxial stresses and smaller lateral confining pressures. Furthermore attention is arbitrarily placed exclusively on the energy dissipating mechanisms associated with the sliding crack model which are commonly considered to be responsible for the major part of the inelastic deformation of compact rock specimens.

In summary, the scope of this initial effort in formulation of a micromechanically based constitutive law for rocks is restricted to plane, laterally confined, brittle deformation of low-porosity (compact) rocks subjected to quasi-static pressure. For some other rocks deforming under different conditions the essential aspects of the constitutive model as discussed within this report will remain basically unchanged. Changes will, however, occur in many details related to different mechanisms of crack nucleation and growth (discussed in Section 2.0) which govern the rock deformation in a particular case.



The mechanical response of a compressed rock specimen containing a large number of sliding cracks which sequentially kink, grow tensile wings, interact with adjacent cracks and form large clusters (shear bands) of coalesced cracks is a complex problem. In general, a "rigorous" micromechanical study of such specimens (Kachanov, 1982; Steif, 1984; Fanella and Krajcinovic, 1988; Nemat-Nasser and Obata, 1988) requires analyses much too complex to be useful in practical applications. The present strategy calls for a less rigorous approach which is only inspired by the micromechanics of the deformation process. In each case, a single representative crack is selected in order to define the proper functional relationship between kinematic and force variables on the macroscale. Consequently, some of the parameters will have to be eventually fitted on the basis of the experimentally measured data. However, in each case, all relevant material parameters will be physically identified in order to enable rational design of an unambiguous experimental program for their determination.

The proposed strategy for the formulation of a phenomenological model has an obvious appeal from a purely practical viewpoint. Material parameters will be identified allowing for requisite experimental measurements. Additionally, phenomenological constitutive models in conjunction with traditional numerical algorithms (finite-element programs) are computationally efficient. Thus, the selected strategy is, indeed, compatible with the organizational scheme of the entire WES directed research and development program. Finally, it seems that the proposed method may even be all that can, and perhaps should, be done at the present time. All "rigorous" micromechanical models include, of necessity, a string of simplifying assumptions which are seldom if ever realistic. For example, even the basic assumption of material homogeneity, used in all existing micromechanical models is, in case of natural materials such as rocks, seldom, if ever, fully justified. Consequently, the accuracy of the "rigorous" models may often be questionable. In view of the required computational effort application of purely micromechanical models may, therefore, not be a rational choice.

## 2.0 MECHANISMS OF COMPRESSION-INDUCED MICROCRACKING IN ROCKS

Rock is a natural, heterogeneous, cohesive material containing several types of inhomogeneities such as microcracks, pores, grain boundaries, joints, second phase inclusions, faults, etc. Under the action of externally applied stresses these flaws become stress concentrators. The ensuing stresses may lead to further degradation of material strength and, finally, to overall brittle failure. In unconfined compression tests, the microcracks grow predominantly in the planes parallel to the direction of loading. The final fracture in the form of splitting (slabbing) is commonly attributed to the unstable growth of several largest, and most favorably oriented cracks that propagate longitudinally towards the specimen's ends. The final failure is abrupt (almost perfectly brittle) and the inelastic strains at failure very small. In contrast, when lateral confinement is present, the deformation process is much more complex since it incorporates both brittle and ductile deformation modes. The final fracture (faulting) in a confined specimen results from the cooperative action of many small defects (cracks) which grow, interact and eventually form a dominant shear fault at some angle to the maximum load axis. Formation of a dominant shear fault implies a failure process which is more gradual and involves substantial dissipation of energy. The stress-strain curve in this case visibly deviates from the straight line and the inelastic and elastic strains at failure are typically of the same order of magnitude.

Several micromechanical mechanisms were proposed in the literature to model the complex process of rock deformation. However, it would be unrealistic to expect that any of those mechanisms can capture all of the salient features observed and reported in experimental studies. The most commonly used models for crack initiation and evolution in rock deformation are briefly summarized below together with appropriate comments on their applicability in rock mechanics.

For highly porous rock, such as some sandstones, the inelastic deformation is commonly attributed to the micromechanism shown in Fig. 2.1. The crack nucleation is attributed to the presence of rather large pores assumed to be spherical in shape. Under external compressive loading at low confining stress  $\sigma_2$ , tensile hoop stresses are generated at the apex of a spherical pore (void). The stress concentration may be further increased by presence of small notches on the pore surface. When the tensile hoop stress near the pore surface (or the notch tip) exceeds the local fracture strength of the material, Mode I (tensile) microcracks develop in the direction of the axial stress  $\sigma_1$  (cf. Sammis and Ashby, 1986).

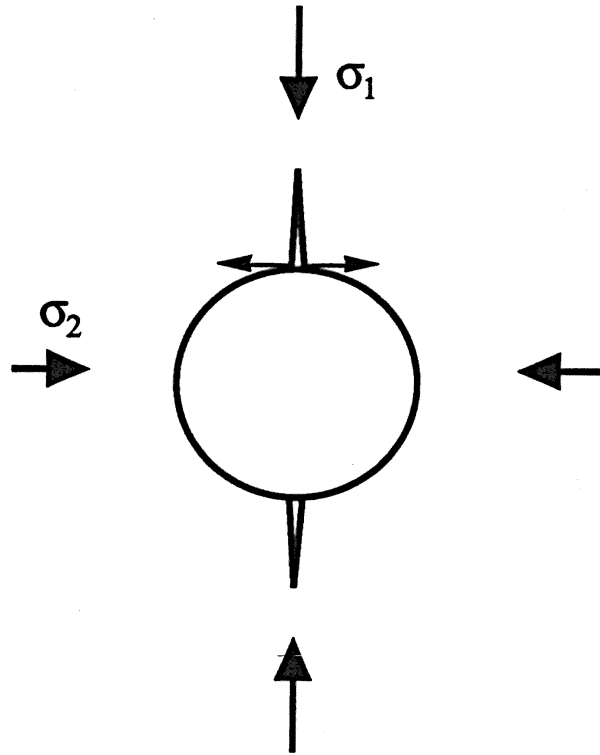


Fig. 2.1. Void (pore) model for crack growth in compression.  
 $\sigma_1$  is the axial and  $\sigma_2$  the confining stress ( $|\sigma_1| \gg |\sigma_2|$ ).

An alternate mechanism to the pore model attributes the inelastic deformation to preexisting closed cracks (slits) in the material. The sliding crack mechanism, shown in Fig.2.2, was used extensively to model the dilatant response of low-porosity rocks (granite) which cannot be explained by the pore model (see, for example, Brace and Bombolakis, 1963, Horii and Nemat-Nasser, 1986, Fanella and Krajcinovic, 1988, Nemat-Nasser and Obata, 1988, Kemeny and Cook, 1991, etc.). The deformation mechanism for low-porosity rocks is much more complex. It involves a succession of events such as frictional sliding, followed by kinking of the original (preexisting) crack and Mode I growth of kinked (wing) segments of the crack. In dependence of the degree of confinement the growth of the kinked parts of the cracks (wings) may be either stable or unstable. In unconfined specimens the ultimate failure occurs as a result of sudden (unstable) growth of a single crack (splitting). The inelastic strain at failure is in this case very small. In the confined case failure is associated with cooperative action of many cracks forming a crack band.



The transition from one mode of failure to the other is commonly referred to as the brittle-to-ductile transition. The details of the deformation process for the case of the sliding crack mechanism will be discussed in sufficient detail later in this report.

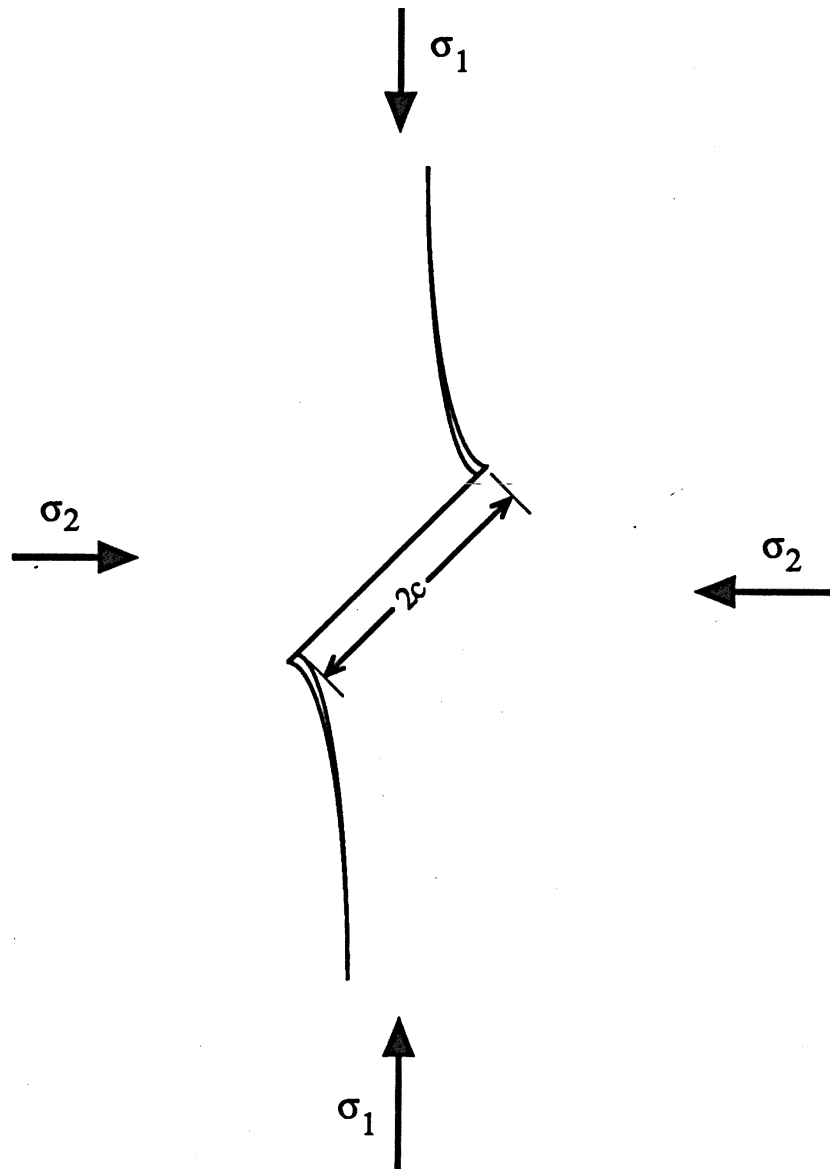


Fig. 2.2. Sliding crack mechanism. The preexisting crack has the length  $2c$ .  $\sigma_1$  is the axial and  $\sigma_2$  the confining stress ( $|\sigma_1| > |\sigma_2|$ ).

Among other brittle mechanisms of microcracking in heterogeneous rocks, the most common are the elastic mismatch mechanism and the bending mechanism. The elastic mismatch model emphasizes the role of the local tensile stresses at the interface of two elastic materials with different elastic moduli ( $E_1 > E_2$ ), e.g. matrix and inclusion. The tensile stresses resulting from the unequal lateral expansions of these two materials often suffice to cause nucleation and subsequent propagation of a microcrack as shown in Fig.2.3a (Kemeny and Cook, 1991). According to the bending model, the tensile stress needed to trigger microcrack growth occurs as a result of bending a soft and elongated particle spanning two harder inclusions, as shown in Fig.2.3b.

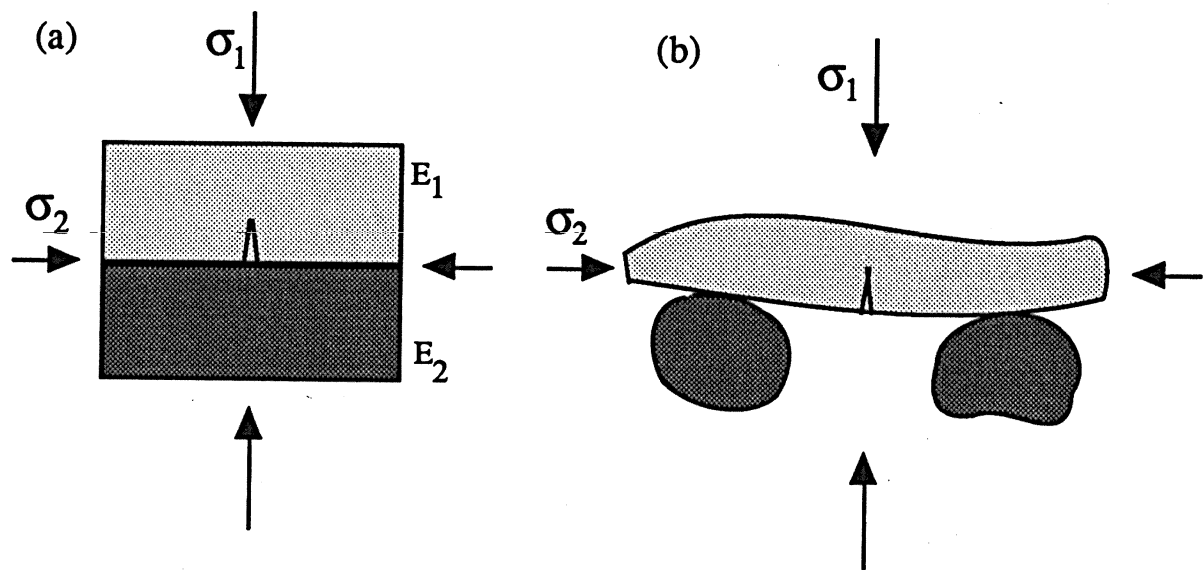


Fig. 2.3 (a) Elastic mismatch model for axial cracking in compression.

(b) Bending model for crack growth under compression.

In both cases the material at the top has inferior stiffness and strength  
and  $|\sigma_1| > |\sigma_2|$ .

The above summary of crack initiating mechanisms is brief rather than exhaustive and comprehensive. Other mechanisms can occur depending on the rock microstructure, loading, temperature, and strain rate.

### 3.0 MICROMECHANICAL BASIS FOR A PHENOMENOLOGICAL DAMAGE MODEL

A two-dimensional phenomenological damage model proposed in this report addresses brittle deformation of low-porosity rocks attributing the inelastic deformation solely to the development of the sliding crack mechanism sketched in Fig.2.2. This mechanism is widely used in the micromechanical modeling of rock inelasticity because of its ability to describe some of the major trends of mechanical behavior observed in experiments. The characteristic aspects observed in compressive tests of low-porosity rock specimens are: large inelastic lateral strain as compared to inelastic axial shortening (resulting in substantial increase of the apparent Poisson's ratio), increasing dilatancy, and dominant effect of the degree of lateral confinement on the failure modes (faulting) and on the ultimate strength of a specimen. Most of these aspects can be explained by the sliding crack deformation model which is, therefore, considered to be the dominant mechanism of inelastic deformation of low-porosity rocks of significant strength. Micromechanical analysis contained in this section summarizes some of the results for the sliding crack model available in the published literature. This micromechanical analysis is used in the formulation of a phenomenological model for the deformation of a low-porosity rock in Section 4.0 of this report. Essential differences between brittle and ductile response of low-porosity, high-strength rocks are listed in Table 3.1 below. The numbers listed in Table 3.1 are typical and may change from one specimen to the other.

Table 3.1. Brittle vs. Ductile Response of Confined Low-Porosity  
Rock Specimens Subjected to Compression

RESPONSE	BRITTLE	DUCTILE
$ \sigma_2 / \sigma_1 $	< 0.1 to 0.2	> 0.1 to 0.2
Failure mode	Slabbing or spalling. Unstable propagation of a single crack.	Coalescence of many small cracks into a crack band.
Inelastic strain at failure	Small compared to elastic strain.	Approximately equal to elastic strain.



### 3.1 Deformation Process.

The entire deformation process of a typical low-porosity rock specimen subjected to compression can be interpreted as a sequence of several distinctly different phases. Since the deformation mechanisms are different in each of these phases, they will be discussed separately in the order of their occurrence. A typical macrostress vs. macrostrain (or better, "force - displacement") curve for a low-porosity rock subjected to a single compressive loading cycle is sketched in Fig. 3.1. Points A to E correspond to the succession of different deformation phases to be discussed in the sequel.

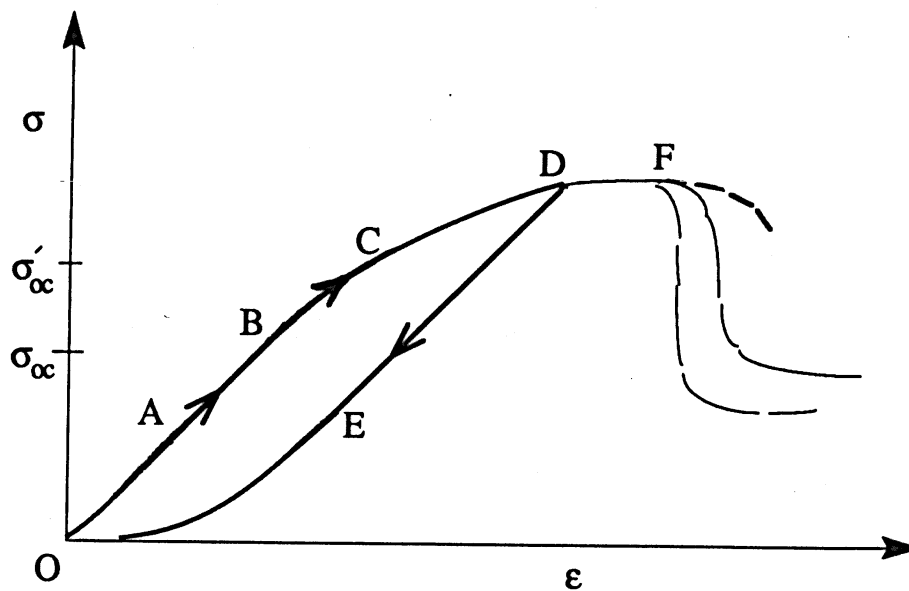


Fig. 3.1. A typical stress-strain curve for a low-porosity rock specimen subjected to uniaxial compression.

*Phase I.* During the initial or first loading phase (segment OB in Fig.3.1) a compact rock usually deforms elastically. In some cases an increase of tangent modulus is observed as a result of crack closure (segment OA in Fig. 3.1). At the current phase of the model development deformation due to the crack closure is neglected, and the rock is assumed to be perfectly elastic. Thus the stress-strain curve in the region OA will be modeled by a straight line. Since a typical

rock contains many crack-like defects this assumption implies that these defects stay closed for the duration of this phase, and that the cracks do not create any discontinuities in the displacement field. Needless to say, during the deformation in Phase I no energy is dissipated since the compaction is elastic.

*Phase II.* Phase II of the deformation process is characterized by the onset of inelastic deformation (point B in Fig. 3.1) attributed to the frictional sliding over the preexisting cracks. During this sliding the cracks do not change their length. In other words, no new internal surfaces are created in the material, and the frictional sliding of the crack faces in a shearing mode is the only energy dissipating mechanism.

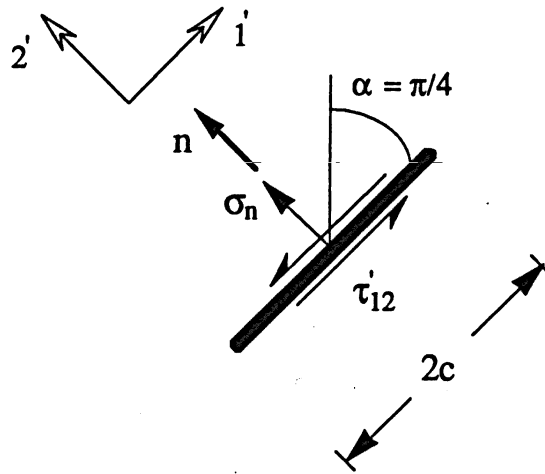


Fig. 3.2. Representative sliding crack before wing formation (Phase II).

For the modeling used in this study, consider first a representative defect. As a representative initial (preexisting) microdefect, select a single, closed, rectilinear microcrack (slit) of length  $2c$  inclined at an angle  $\alpha = \pi/4$  with respect to the direction of principal compressive stress  $\sigma_1 > \sigma_2$ , Fig. 3.2. The matrix surrounding the rectilinear slit is assumed to be homogeneous, isotropic and elastic. Compressive stress and shortening are assigned positive sign. The resolved shear and normal stresses acting on the crack faces are

$$\begin{aligned}\tau'_{12} &= (1/2)(\sigma_1 - \sigma_2)\sin 2\alpha = \frac{1}{2}(\sigma_1 - \sigma_2) \\ \sigma'_2 &= \sigma_n = (1/2)[(\sigma_1 + \sigma_2) - (\sigma_1 - \sigma_2)\cos 2\alpha]\end{aligned}\tag{3.1}$$

where prime indicates local (crack) coordinate system. The axis  $2'$  is colinear with the normal  $n$  (Fig. 3.2) to the slit.

During Phase I of the deformation process the slit is closed and resists relative displacement of its faces. At the onset of Phase II the resolved shear stress  $\tau'_{12}$  exceeds the frictional and cohesive resistance at the crack interface triggering relative sliding of the two crack faces in contact. Assuming a Mohr-Coulomb type relationship the effective (or net) shear stress responsible for the relative motion (frictional sliding) of the slit faces (attached to each other only at crack tips) is

$$\tau_{\text{eff}} = \tau'_{12} - (\mu\sigma'_2 + \tau_c) > 0\tag{3.2}$$

As soon as the inequality (3.2) is satisfied, during the loading process, frictional sliding will begin (point B in Fig. 3.1). The onset of inelastic deformation associated with frictional sliding is reflected in the initial deviation of the stress-strain curve from the straight line shown in Fig. 3.1. In (3.2),  $\mu$  is the coefficient of friction (assumed to be constant),  $\tau_c$  is the current value of cohesive shear strength of the matrix. A preexisting slit may also be curved or locked by a hard particle. These cases would require appropriate changes of the sliding condition (3.2). The shear resistance to a large degree depends on the roughness of the slit faces, i.e. interlock of surface asperities. Thus, in the case of cyclic loading it seems reasonable to assume that the shear resistance will decrease with each loading cycle as these asperities are sheared away. The slit length  $2c$  remains constant during Phase II (segment BC of the stress-strain curve shown in Fig. 3.2) of the deformation process.

*Phase III.* Once the frictional sliding is initiated (and the inequality (3.2) satisfied), the considered crack is subjected to Mode II loading. In other words, the singular stress field at the crack tip acting as stress concentrator, is dominated by the  $K_{II}$  stress intensity factor. At some point the maximum energy release rate  $G(\theta) = K_{II}^2 / E$  will reach the threshold or critical value (characterizing material toughness) in a plane at an angle  $\theta$  with the original slit. The stresses in the vicinity of the crack tip are linear and homogeneous functions of the stress intensity factors. Thus, the critical value of the energy release rate can also be interpreted as a critical value of the maximum tensile hoop stress in the vicinity of the crack tip. Regardless of interpretation, at this point the slit



will suddenly sprout a wing crack at each tip (point C in Fig. 3.1). This wing crack will be at an angle  $\theta$ , subtending approximately an angle of 70 degrees\* (Fig. 2.2) with the direction of the original slit. As the wing crack grows from the near-field of the initial slit (wing length is small in comparison to the length of the preexisting slit,  $\delta L \ll c$ ), dominated by the stress intensity factor, into the far-field of the macrostresses (wing length is larger than the length of the original slit,  $\Delta L > c$ ) the crack shifts from a mixed-mode (coupling Mode I and Mode II) to a single-mode ( $K_I > 0$ ,  $K_{II} = 0$ ) tensile or cleavage loading (Lawn and Wilshaw, 1975). The actual orientation of the original slit is important only during the initial phase of the wing growth ( $L \ll c$ ). After a short initial curved segment, the wings will align themselves with the compressive stress  $\sigma_1$  and become rather straight.

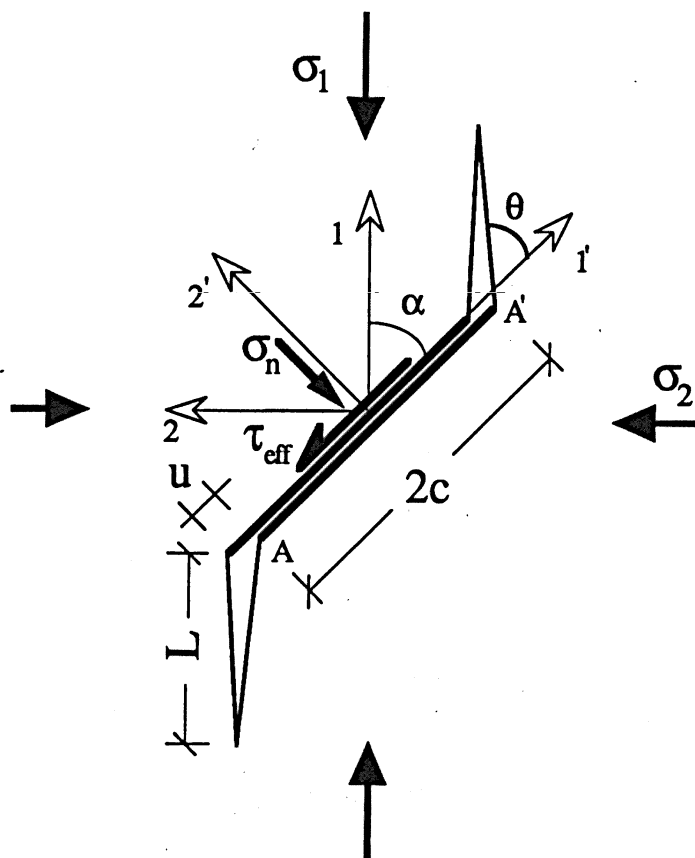


Fig.3.3 Sliding crack mechanism with simplified wing geometry. The applied stresses and forces on the crack and the gap opening displacement  $u$  are shown as well.

\* A Table of factors for converting non-SI units to SI (metric) units is presented on page iii.

Having in mind the relative insensitivity of wings on the actual direction and even size of the original slit, it is sufficient to consider a representative kinked crack sketched in Fig. 3.3. The original slit is at an angle of 45 degrees with respect to principal macrostresses  $\sigma_1$  and  $\sigma_2$ . The wing cracks which are slightly curved, according to the linear elastic fracture mechanics theory based on the assumption that the matrix is homogeneous, are approximated in subsequent analysis by straight lines colinear with the principal compressive macrostress  $\sigma_1$ . The heterogeneity of the rock, i.e. inhomogeneous distribution of fracture strength across the volume, has a strong influence on the shape of the crack. Thus, the nicely curved wings (Fig.2.2), obtained from theoretical analyses assuming homogeneous material, are never observed in natural rock formations or even experimental specimens. Consequently, simplifying the wing crack geometry (Figs.2.2 and 3.3) to make the model tractable is more than justified.

The two sources of inelastic strains occurring during Phase III (region between points C and D in Fig. 3.1) of the deformation process are the displacement discontinuities associated with the openings of wing cracks, and the frictional sliding across the faces of the preexisting slit. Assuming that the directions of macro (average) stresses do not rotate and strains remain small during the entire deformation process, the total strain tensor  $\epsilon$  can be decomposed into four component tensors

$$\epsilon = \epsilon^v + \epsilon^e + \epsilon^f + \epsilon^c \quad (3.3)$$

where  $\epsilon^v$  is the strain due to the initial compaction of pores,  $\epsilon^e = S:\sigma$  is the elastic deformation of the matrix (with  $S$  being the compliance tensor depending on the already accumulated damage),  $\epsilon^f$  is the strain due to frictional slip of preexisting cracks and  $\epsilon^c$  is the strain due to the opening of the wing cracks. The original, preexisting crack remains closed and contributes to inelastic deformation exclusively through the frictional slip. Additional strains due to thermal effects, chemical reactions, pore pressure, etc. may be added to the right-hand side of the expression (3.3) for the total strain.

*Phase IV.* Assuming that the macrostrength of the specimen was not exceeded, the final phase of the deformation process consists of unloading (segment DE of the stress-strain curve in Fig. 3.1). In the course of quasi-static unloading (starting at the point D in Fig. 3.1), the material response is initially linearly elastic up to a point E. In general, the axial elastic modulus in the region DE will be slightly reduced in comparison with its initial value measured from the slope of the segment AB of the stress-displacement curve. This results from the fact that following the

loading cycle to the point D the rock specimen becomes more compliant due to additional microcracking. However, for the assumed representative kinked crack (Fig. 3.3), consisting of the preexisting slit oriented at 45 degrees and straight vertical wings parallel to the axial compressive stress  $\sigma_1$ , the elastic modulus in unloading (DE) is assumed to remain virtually the same as for the segment AB of the stress-strain curve. During the elastic unloading, all the preexisting slits are locked and the wing cracks remain open. At the point E, the backsliding on some preexisting flaws commences.

The initiation of the backsliding process can be determined in the following way. Denote by  $\tau_{\text{eff}}^m$  the maximum effective elastic shear stress stored in the material (corresponding to the stress state at the point D in Fig. 3.1) surrounding the crack faces during the loading process. If the unloading starts, this stress acquires the opposite sign. The condition for the onset of the reverse sliding becomes (e.g. Jaeger and Cook, 1979)

$$\tau_{\text{eff}}^m \geq \tau'_{12} + \mu \sigma_n \quad (3.4)$$

where  $\tau'_{12}$  and  $\sigma_n$  are current values of the shear and normal stress acting on the preexisting crack, Fig. 3.3. As soon as the unloading commences the direction of the frictional resistance changes its direction as well. The effective shear stress acting on the face of the inclined part of the kinked crack (Fig. 3.3) is

$$\tau_{\text{eff}}^m = \tau'_{12}^m - \mu \sigma_n^m \quad (3.5)$$

where superscript m denotes stresses at the peak of the preceding cycle (point D in Fig. 3.1). Note that in (3.5) the cohesive shear stress,  $\tau_c$ , vanishes at the peak of the  $\sigma$ - $\epsilon$  curve. Denote further the reduction in normal and shear stresses (taken with respect to the corresponding stresses at point D in Fig. 3.1) by

$$\sigma_n^m - \sigma_n = \Delta \sigma_n, \quad \tau'_{12}^m - \tau'_{12} = \Delta \tau'_{12} \quad (3.6)$$

Introducing (3.5) and (3.6) into the condition for backsliding initiation (3.4) leads to

$$\Delta \tau'_{12} + \mu \Delta \sigma_n \geq 2\mu \sigma_n^m \quad (3.7)$$

According to the inequality (3.7), the reverse sliding will start if the drop in the shear stress and reduction of frictional resistance along the crack faces exceeds the threshold value  $2\mu\sigma_1^m$ . In the case of the uniaxial compression ( $\sigma_1 \neq 0$ ,  $\sigma_2 = 0$ ), the reverse sliding condition (3.7) reduces, for the crack angle of 45 degrees, to a much simpler form

$$\Delta\sigma_1 \geq \frac{2\mu}{1+\mu} \sigma_1^m \quad (3.8)$$

where  $\sigma_1^m$  denotes the maximum compressive stress applied to the specimen in loading (point D in Fig. 3.1).

The permanent (residual) strain that remains in the specimen after a complete unloading (i.e. when the externally applied stress  $\sigma$  is reduced to zero) is commonly attributed to the imperfect crack closure and to a lesser extent to the plastic strains in the vicinity of the tips and kinks of the crack shown in Fig.2.2 (if the lateral confinement was present). Determinations of the permanent strains were considered to be beyond the scope of the initial phase in the model development.

*Softening Regime.* Finally, in certain cases it becomes necessary to consider the softening (descending) part of the stress-strain curve (beyond apex F sketched by dashed lines in Fig. 3.1), i.e. the part of the curve for which the tangent modulus becomes negative. These analyses are rather difficult and the deformation process is still not well understood. In consideration of the deformation processes developing in the course of all phases preceding softening it was tacitly assumed that the defects are small in comparison with the specimen and that the distribution of defects is such that the specimen can be considered macrohomogeneous (i.e. homogeneous in a statistical sense). These assumptions are not valid in the case of softening. Softening deformation of the specimen is dominated by the largest cluster of coalesced defects (macrocrack). This cluster, in general, has a random geometry, which in an essential manner, depends on the details of the microstructure and the initial distribution of microdefects. Consequently, the mechanical response during this phase of the deformation is strongly influenced by the higher statistical momenta (statistically unlikely events) of the initial defect distribution. Correspondingly, the purely deterministic models of softening (or post-localized response) available in the existing literature are of dubious merit. The deformation beyond the apex of the stress-strain curve is not considered in this report.

### 3.2. Strain - Displacement Relations

The principal objective of the micromechanical studies, presented within this section, is to investigate the relations between the displacement discontinuities imposed by cracks and the overall (macro) strains. In a rigorous micromechanical analysis this task involves, in addition to the following development, a homogenization (averaging) procedure in order to estimate the contributions of all microdefects within a representative volume element. Consequently, this procedure involves a nontrivial computational effort even in the case of homogeneous stress and strain fields. In the case of nonhomogeneous stress and strain fields the data bank containing all relevant information regarding microdefects in each material point of the specimen is too large to be manageable in practical applications (see Krajcinovic, 1989). Thus, in view of the stated objectives, the task is herein somewhat simplified considering only a single, representative crack and its contribution to the macrostrains.

*Inelastic Strains Attributed to Frictional Sliding.* The inelastic strains associated with the relative frictional slip of the faces of a closed rectilinear slit, can be computed by the method suggested in the Nemat-Nasser and Obata (1988) model. In general, the strains due to discontinuities of the displacements (in any mode)  $u$  along a surface  $(-a \leq \ell \leq a)$  with normal  $n$ , can be, using the conventional divergence theorem, readily written in the form

$$\epsilon_{ij}' = (N/2) \int_{-a}^a (n_j' u_i' + n_i' u_j') d\ell \quad (3.9)$$

where  $N$  is the crack density (number of cracks in a unit volume) and the integration extends over the entire surface (or in this case, length) of the discontinuity.

During the course of Phase II of the deformation process the inelastic strains are attributed solely to the frictional sliding ( $\epsilon^f \neq 0$ ,  $\epsilon^c = 0$ ). Assuming that the initial rectilinear crack (slit) is closed and remains closed throughout the entire process of sliding, it follows from (3.9) that in the local (crack) coordinate system  $(1', 2')$  the macrostrains associated with frictional sliding are

$$\epsilon_{11}' = \frac{N}{2} \int_{-c}^c (n_1' u_1' + n_1' u_1') da \quad \epsilon_{22}' = \frac{N}{2} \int_{-c}^c (n_2' u_2' + n_2' u_2') da \quad (3.10 a)$$

$$\epsilon_{12}' = \epsilon_{21}' = \frac{N}{2} \int_{-c}^c (n_1' u_2' + n_2' u_1') da = N \int_0^c u_1' da = Nuc \quad (3.10 b)$$

In expressions (3.10)  $n_1' = 0$  and  $u_2' = 0$  since the slit is rectilinear with normal  $n_2'$  and the only displacement discontinuity is attributed to sliding motion  $u_1'$  in the direction of the coordinate axis 1'. Since the present analysis is two-dimensional,  $N$  in the formulas (3.10) denotes the number of cracks per unit area. Consequently,  $N$  is the property of the specimen reflecting the degree of damage existing in the specimen prior to the considered loading. The average slip  $u$  (Fig.3.3) is determined averaging the Mode II crack opening displacement over the crack length. In the global coordinate system (1, 2) the strain tensor due to sliding takes the form

$$\epsilon_{ij}^f = \epsilon_{12}' \begin{bmatrix} 1 & 0 \\ 0 & -1 \end{bmatrix} = \frac{fu}{c} \begin{bmatrix} 1 & 0 \\ 0 & -1 \end{bmatrix} \quad (3.11)$$

where  $f = Nc^2$  is a parameter characterizing crack size and density. The equations (3.11) are obtained from (3.10) using coordinate transformation from the primed (slit) to the fixed (global) coordinate system.

*Strains due to microcracking.* During Phase III of the deformation process the relative sliding of the faces of the preexisting crack is coupled with the growth of tension wing cracks, so that  $\epsilon^f \neq 0$ ,  $\epsilon^c \neq 0$ . The onset of cracking (point C in Fig. 3.1) is defined by Griffith's instability condition at the crack tip

$$G = G_c \quad (3.12)$$

where  $G$  is the elastic energy release rate, and  $G_c$  is the critical elastic energy release rate and is a material parameter defining the fracture toughness of the rock specimen. Unfortunately,  $G_c$  is not always a constant and is dependent on several aspects of the geometry and state of stress. Initially, the energy release rate  $G$  is associated with the frictional sliding on the preexisting slit, i.e. Mode II loading.

Consider first the relation between the macrostrains and the displacement discontinuities imposed by the kinked crack shown in Fig. 3.3. Relative sliding of the faces of the preexisting crack creates concentrated discontinuities (gaps) at the points A and A'. Opening of the wings due to the gaps created by the sliding crack faces contributes to the global strain  $\epsilon^s$  as (see, for example, Nemat-Nasser and Obata, 1988)

$$\epsilon_{ij}^g = \frac{1}{2} \frac{u}{c} \frac{L}{c} \begin{bmatrix} 0 & \sqrt{2}/2 \\ \sqrt{2}/2 & -\sqrt{2} \end{bmatrix} \quad (3.13)$$

The lateral stresses  $\sigma_2$  (assumed to be compressive) resist this opening displacement of the wing cracks. The resulting strain associated with the resistive action of lateral stresses is (see again Nemat-Nasser and Obata, 1988)

$$\epsilon_{ij}^a = f \frac{1 - \nu^2}{4E} \frac{\pi L^2}{c^2} \begin{bmatrix} 0 & 0 \\ 0 & \sigma_{22} \end{bmatrix} \quad (3.14)$$

where  $\nu$  is the Poisson's ratio and  $E$  the elastic modulus. The component of the total strain related to the average crack opening displacements (3.13) and (3.14) is  $\epsilon_{ij}^c = \epsilon_{ij}^g + \epsilon_{ij}^a$ .

### 3.3. Stress - Displacements Relationship

The ultimate objective of this exercise is to derive a relation between the macrostrains and macrostresses in a rock specimen under considered loading conditions. In the preceding section, the strains were derived in terms of the average displacement discontinuities  $u$ . Hence, the next task consists of the determination of relations between the displacement discontinuities  $u$  and macro-stresses  $\sigma$ . In general, this task involves application of the methods of linear elastic fracture mechanics. Most of the expressions to be used in this section are available in collections of expressions for the stress intensity factors such as that by Murakami (1987) and others.

*Frictional Sliding of the Faces of the Preexisting Rectilinear Slit.* Consider first the relative Mode II sliding of the two faces of the preexisting crack subjected to effective shear stress. In this case the displacement discontinuity occurs only in the direction of the slit plane. Since the slit is fixed at two ends, the displacement discontinuity must be averaged over the length of the slit,

$$u_1' = \frac{16(1-\nu^2)}{\pi E(2-\nu)} \tau_{\text{eff}} \frac{1}{2c} \int_{-c}^c (c^2 - x^2)^{1/2} dx = \frac{4(1-\nu^2)}{E(2-\nu)} c \tau_{\text{eff}} \quad (3.15)$$

Combining (3.11) and (3.15) it becomes possible to relate the macrostresses and macrostrains by eliminating the displacement discontinuity  $u$ .



**Kinked Crack.** In order to compute the strains from (3.13) and (3.14) it is necessary to determine the amount of average slip  $u$  and the size of the wing crack  $L$  as a function of macro-stresses. Both of these quantities can be determined if the stress intensity factor  $K_I$  at the tip of the kinked crack is known.

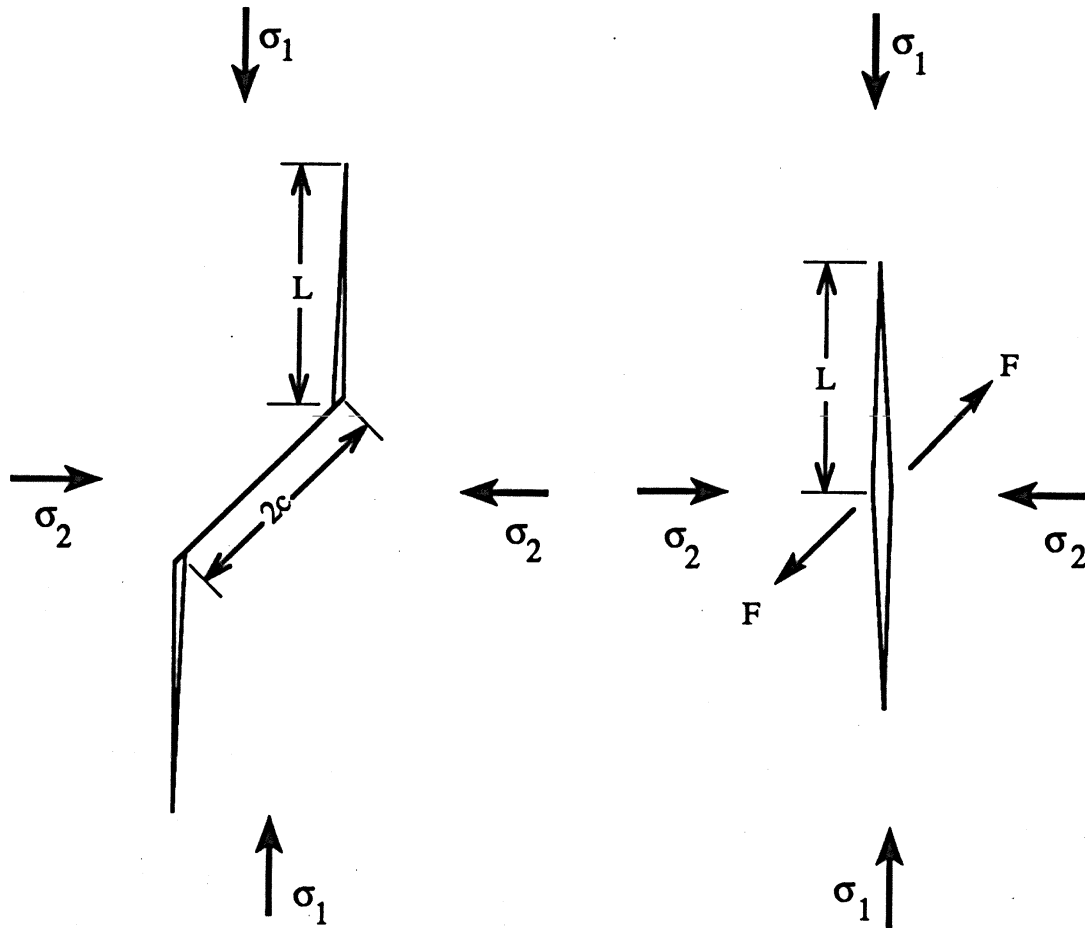


Fig. 3.4. Actual kinked crack and substitute rectilinear crack.

The stress intensity factor  $K_I$  at the tip of the wing crack can be computed from deformations and forces. However, a closed form, analytical solution for the stress intensity factor of the actual, kinked geometry is not possible. Approximating the actual crack by a rectilinear crack as shown in Fig. 3.4 and subjecting it to concentrated forces  $F = 2c\tau_{\text{eff}}$  at the crack center and lateral uniformly distributed stresses  $\sigma_2$ , Horii and Nemat-Nasser (1986) were able to compute the stress intensity factor  $K_I$  as

$$K_I = \sqrt{2/\pi} \frac{c}{\sqrt{L + L^*}} \tau_{\text{eff}} - \sigma_2 \sqrt{\pi L} \quad (3.16)$$

where,  $L^*$  is included to render  $K_I$  nonsingular when  $L \rightarrow 0$ . The constant  $L^*$  can be computed from the condition that  $K_I$  given by (3.16) in the limit as  $L \rightarrow 0$  reduces to the solution by Cotterell and Rice (1980) for a kink initiation. In the present case ( $\alpha = 45$  degrees) it follows that

$$\frac{L^*}{c} = \frac{32}{9\pi^2 [\sin(\pi/8) + \sin(3\pi/8)]^2} = 0.21 \quad (3.17)$$

Numerical computations for a crack of actual (kinked) configuration demonstrate surprising accuracy of the expression (3.16) developed for the substitute rectilinear crack sketched in Fig. 3.4.

Alternatively, the stress intensity factor  $K_I$  at the tip of the wing crack can be determined assuming that the crack is wedged open at the wing root by displacement  $u$  (relative sliding along the preexisting slit). In this case the stress intensity factor  $K_I$  is

$$K_I' = \frac{\sqrt{2}G_0}{2(1 - \nu_0)} \frac{u}{\sqrt{2\pi(L + L^{**})}} - \sigma_2 \sqrt{\frac{\pi L}{2}} \quad (3.18)$$

where  $L^{**}$  plays the same role as  $L^*$  in (3.16) and was found to be  $(L^{**}/c) = (\pi^2/32)(L^*/c) = 0.065$ . The first term on the right-hand side of (3.18) reflects the contribution of wedging, while the second term defines the resistive role of the lateral confining pressure.

Expressions (3.16) and (3.18) represent the same quantity. Thus,

$$K_I' = K_I \quad (3.19)$$

whenever the sliding activation condition (3.2) is satisfied.

Substituting expressions (3.16) and (3.18) into (3.19) it was possible to derive the expression for the average slip along the preexisting crack as a function of the applied stresses

$$u = 2c \frac{1-\nu_o}{G_o} \left[ \sqrt{2 \frac{(L/c) + (L^{**}/c)}{(L/c) + (L^*/c)}} \tau_{\text{eff}} - \sigma_2 \pi (1 - \sqrt{2}/2) \sqrt{(L/c) [(L/c) + (L^*/c)]} \right] \quad (3.20)$$

The length of the wing crack can be obtained from the Griffith condition (3.12). The ensuing expression can be arranged in the form of a rather complicated fourth-order algebraic equation which cannot be solved in a closed form

$$\left(\frac{\hat{L}}{2}\right)^2 \left(K_{IC} + \frac{1}{K_{IC}} \pi L \sigma_2^2\right)^2 - \sigma_2^2 \pi L \hat{L}^2 - \frac{c}{\pi K_{IC}} \tau_{\text{eff}}^2 \hat{L} \left[K_{IC} + \frac{1}{K_{IC}} \pi L \sigma_2^2\right] + \left(\frac{2c}{\pi K_{IC}}\right)^2 = 0 \quad (3.21)$$

where  $\hat{L} = (L/c) + (L^*/c)$ . However, since  $(L^*/c) \ll (L/c)$  for long wings,  $(L^*/c)$  can be neglected at latter stages of the deformation process (i.e., when the inelastic deformation is more pronounced). In this case, the aspect ratio  $(L/c)$  can be derived from the expression (3.21) in the form of a simpler expression

$$\frac{L}{c} = \frac{K_{IC}^2 + 2\sqrt{2}c\tau_{\text{eff}}\sigma_2 - K_{IC}\sqrt{K_{IC}^2 + 4\sqrt{2}c\tau_{\text{eff}}\sigma_2}}{2\pi c\sigma_2^2} \quad (3.22)$$

Having determined the average slip and the kink length as functions of stresses, it becomes possible to compute the macrostrains from (3.11), (3.13) and (3.14). As is always the case in micromechanical modeling, all material constants involved have a clear and well-defined physical meaning allowing unambiguous experimental identification. In the case considered here these material parameters are: elastic constants, fracture toughness  $K_{IC}$ , average initial preexisting crack length  $c$ , and initial crack density parameter  $f = Nc^2$  for a specific rock sample.

## 4.0 PHENOMENOLOGICAL MODEL

The micromechanical analysis of the preceding section will now be used as a background to formulate a phenomenological constitutive model for the inelastic behavior of a brittle rock under compression. For the assumed cracking mechanism and the crack configuration shown in Figs. 2.2 and 3.3, it directly follows that nonlinear axial strain can be attributed primarily to the sliding on preexisting cracks. The lateral strain, however, can be traced both to sliding and opening of the wing cracks and is, therefore, more pronounced than the axial shortening of the specimen. This fact is corroborated by existing experimental data for hard rocks such as granite (e.g. Zoback and Byerlee, 1975). The same conclusion is, however, not always true for concrete (see, Krajcinovic, et al. 1991) and may, therefore, be questionable in the case of porous rocks as well. The faces of the sliding crack were assumed to remain in contact throughout the entire process of deformation. Therefore, the microstructural origins of rock dilatancy under compressive stresses are, in the proposed model, the result of the crack opening displacements of the wing cracks. Since the frictional sliding of the faces of the preexisting cracks does not involve any volume change of the material, the resulting deformation can be modeled using conventional methods of the theory of plasticity. In the case when the crack surfaces are very rough, frictional sliding over large asperities may result in volumetric changes, especially during the first few loading cycles. In this case, the present model will have to be appropriately modified.

In the absence of experimental results it seems reasonable to start with the simplest version of the analytical model. However, in the considered case the deformation process emphasizes interaction of two different modes of irreversible changes of the microstructure. Mechanical energy is, in other words, dissipated on frictional sliding and microcracking (creation of new internal surfaces in the specimen). It will be assumed that the relation between the thermodynamic fluxes and their affinities (conjugate thermodynamic forces) for the two energy dissipating mechanisms can be formulated on the basis of appropriately defined potential functions.

### 4.1 Nondilatant Frictional Sliding

As already mentioned, prior to any growth (kinking) the preexisting crack is, during Phase II of the deformation process, subjected to frictional (and cohesive) forces along its faces. If the normal opening of such a crack is neglected ( $u_2' = 0$ ), no inelastic volume change of the material

will take place and the ensuing deformation will be solely attributable to the relative frictional sliding of the faces of activated cracks. This process is, to a large extent, analogous to slip along the slip planes in polycrystalline materials. Consequently, standard methods of  $J_2$  plasticity theory can be used to evaluate macroscopic strains in Phase II of the deformation process. In the case when a perfect contact between the faces of the crack exists in the direction of the crack normal, the analysis suggested by Rudnicki and Rice (1975) and extended by Nemat-Nasser and Shokooh (1980) could be adopted, or at least properly modified. In these papers the normality rule is relaxed and nonassociative flow is introduced.

According to earlier studies by Rudnicki and Rice (1975) appropriate modeling of internal frictional sliding requires use of a nonassociative flow rule. The angle subtended by the plastic flow vector and the normal to the yield surface is an additional material parameter associated with frictional resistance. The nonassociative flow rule is especially important in studies of localization, a process during which the slips self-organize into a shear band (Rudnicki and Rice, 1975). It was shown by Rudnicki and Rice (1975) that a  $J_2$  plasticity theory must be embellished either by introducing vertices into the yield surface or by relaxing the normality rule in order to be able to predict the onset of localization. In the case considered in this report plastic strain attributable to frictional sliding over the preexisting slits is neither the only nor the dominant source of inelasticity. Thus, it seems reasonable to start with the associative rule and ascertain the limits of its validity. However, if the subsequent developments demonstrate that the nonassociative model is absolutely necessary the requisite modifications will have to be incorporated into the present model.

In the present model (based on the slanted preexisting crack shown in Fig. 3.2. and the kinked crack shown in Figs. 3.3 and 3.4) the volumetric changes are exclusively due to the displacement discontinuities (crack opening displacements) across the wings. Therefore, for the determination of strains in Phase II, it suffices to introduce a scalar-valued parameter  $\hat{h}$  defining the hardening due to distortional plastic work. In general, this parameter, for incompressible plastic deformation and constant lateral pressure, can be expressed, as suggested by Nemat-Nasser and Shokooh (1980), as

$$\hat{h} = (\partial q / \partial \epsilon^f) \quad (4.1)$$

where

$$q = \sigma_1 - \sigma_2 = 2\sqrt{J_2} \quad (4.2)$$

is the differential stress for a two-dimensional case and  $J_2$  is the second invariant of the deviatoric stress tensor. The distortional strain  $\epsilon^f$  is

$$\epsilon^f = (1/2)(\epsilon_1 - \epsilon_2) \quad (4.3)$$

where  $\epsilon_1$  and  $\epsilon_2$  are the principal components of the plastic strain tensor. Note that in the considered case ( $\alpha = 45$  degrees)  $\epsilon_1 = -\epsilon_2$ . Usually the variation of the distortional hardening parameter with strain (4.1) is assumed on the basis of experimental observations. It is well known that the hardening parameter  $\hat{h}$  must be a monotonically decreasing function of  $\epsilon^f$ . The particular form of the functional relationship  $h(\epsilon^f)$ , though, will be dependent on the specific rock. For the purpose of illustration of a possible phenomenological model, assume that for constant lateral confining stress  $\sigma_2 = \text{constant}$

$$(d\sigma_1/d\epsilon^f) = h(\epsilon^f)^{-1/n} \quad (4.4)$$

where  $h$  and  $n$  are material parameters to be determined from experiments. Integrating (4.4) it follows that

$$\epsilon_1^f = \epsilon_2^f = \epsilon_{uc}^f \left( \frac{\sigma_1 - \sigma_{oc}}{\sigma_{uc} - \sigma_{oc}} \right)^{n/(n-1)} \quad (4.5)$$

where  $\sigma_{uc}$  denotes the ultimate strength in uniaxial compression, while  $\epsilon_{uc}^f$  is the corresponding strain due to sliding at the apex (to be determined in Section 5.0). The stress  $\sigma_{oc}$  at the onset of sliding is obtained from the slip activation condition (3.2) as

$$\sigma_{oc} = \frac{2\tau_c^0 + \sigma_2(1 + \mu)}{1 - \mu} \quad (4.6)$$

where  $\tau_c^0$  is the initial cohesive shear strength of the material and  $\mu$  the friction coefficient.

## 4.2 Microcracking

Next consider Phase III of the deformation process during which both sliding and microcracking occur simultaneously. The approximate formula (3.16) (Horii and Nemat-Nasser, 1986) for the stress intensity factor was based on the assumption that the representative crack in Fig. 3.3 subjected to macrostresses  $\sigma_1$  and  $\sigma_2$  is equivalent (i.e. has identical stress intensity factor  $K_I$ ) to a straight vertical crack of length  $2L$  subjected to the applied stresses  $\sigma_1$ ,  $\sigma_2$  and to a pair of colinear concentrated splitting forces  $F = 2c\tau_{\text{eff}}$  oriented along the direction of the preexisting part of the sliding crack. These concentrated forces were to represent the effect of sliding along the slanted crack upon opening of the wing cracks. If a single crack is considered, this simplification provides a reasonably good estimate for the stress intensity factor  $K_I$  with the lateral strain  $\epsilon_2$  and the shear strain  $\epsilon_{12}$  being the only non-zero (inelastic) strain components (see expressions 3.13 and 3.14).

In the formulation of a phenomenological damage model, the effect of symmetry in crack orientation has to be taken into account. In the case of a rock specimen weakened by a random population of many preexisting cracks, there is an equal chance for a slanted representative crack to be oriented either at  $\alpha = \pi/4$  or  $\alpha = (\pi - \pi/4)$ , Fig. 4.1a. In other words, there are just as many cracks at an angle of  $\alpha = \pi/4$  as there are cracks at an angle of  $\alpha = (\pi - \pi/4)$ . In this case, considering pairs of cracks, the shear macrostrains vanish since the shear components of the splitting forces  $F$  on two cracks constituting a pair cancel each other (see Fig. 4.1b). Consequently, the lateral normal strain  $\epsilon_2$  remains the only non-vanishing component of the inelastic strain tensor attributed to microcracking. For this reason it is postulated that a single vertical crack subjected to a yet undefined lateral tensile stress  $\sigma_2''$  can be used to determine the strains due to microcracking, as shown in Fig. 4.1c. In consequence, the lateral compliance ( $S_{22}$ ) increases as the cracks grow in size, while all other components of the compliance tensor  $S$  remain virtually unchanged.

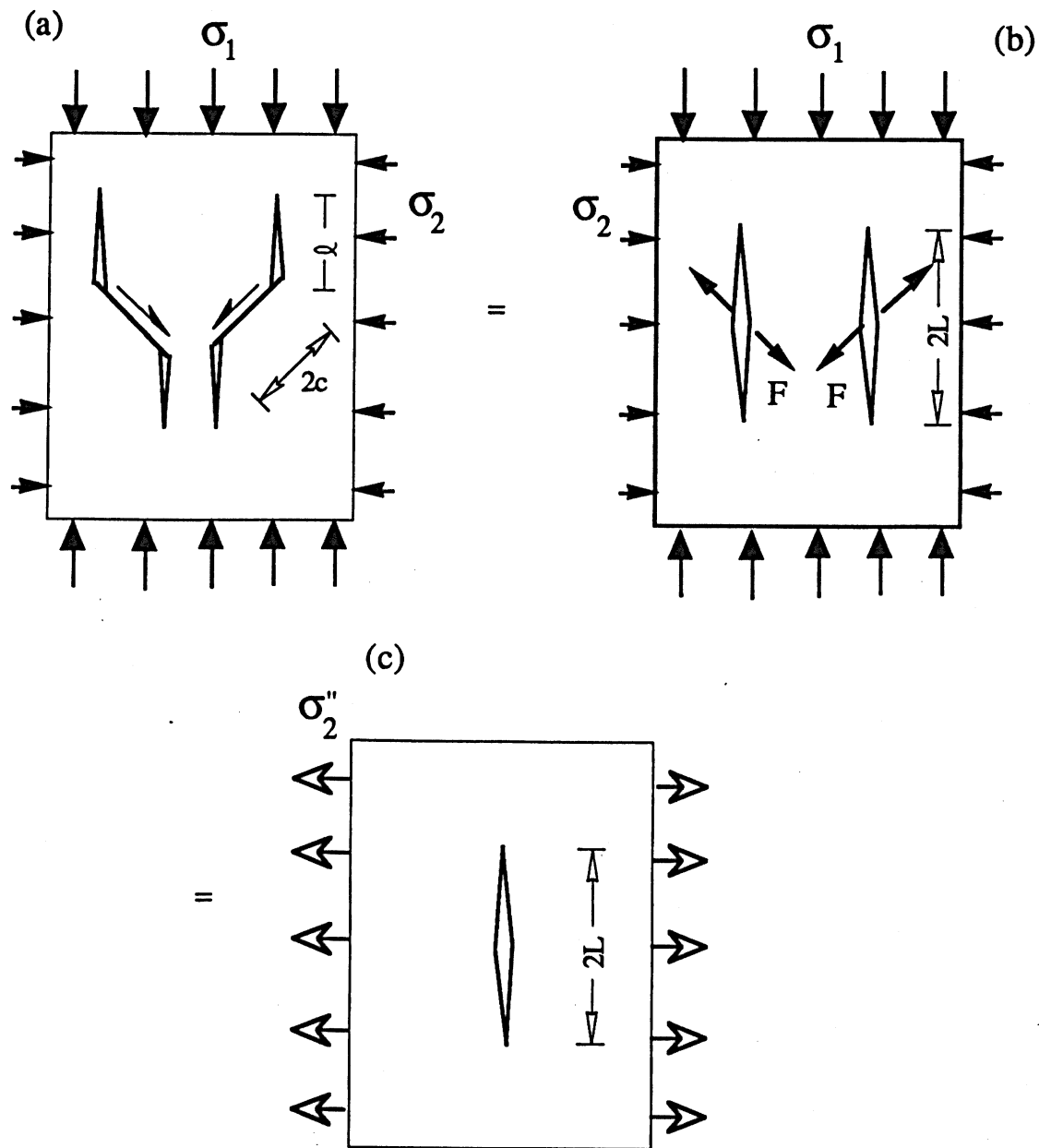


Fig.4.1.(a) Symmetric pair of representative cracks.

(b) Equivalent cracks for calculation of  $K_I$  from (3.16).

(c) Configuration used in the proposed phenomenological model.



The stress intensity factor (3.16) for the rectilinear crack shown in Fig. 4.1c can now be expressed in a simple form as

$$K_I = \sigma_2'' \sqrt{\pi L} \quad (4.7)$$

where

$$\sigma_2'' = b(L) \tau_{\text{eff}} \quad (4.8)$$

$$b(L) = \frac{\sqrt{2}}{\pi} \left[ \sqrt{(L/c)^2 + (L/c)(L^*/c)} \right]^{-1} \quad (4.9)$$

$$\tau_{\text{eff}} = \frac{1}{2} [\sigma_1(1 - \mu) - \sigma_2(1 + \mu)] - \tau_c \quad (4.10)$$

It is notable that the expression (4.7) for the stress intensity factor  $K_I$  predicts stable crack growth when the Griffith condition (3.12) is met, since the derivative

$$\frac{\partial K_I}{\partial L} = - \frac{c}{\sqrt{2\pi}} \frac{\tau_{\text{eff}}}{(L+L^*)\sqrt{L+L^*}} - \frac{\sigma_2''}{2\sqrt{\pi L}} \quad (4.11)$$

is negative when the lateral stress  $\sigma_2''$  is compressive (positive). In other words, an increase in the crack size ( $dL$ ) results in the decrease of the crack "driving force" ( $dK_I$ ). However, in the presence of lateral tension ( $\sigma_2'' < 0$ ) the crack growth could be unstable since, above a threshold level of  $\sigma_2''$  the derivative ( $\partial K_I/\partial L$ ) given by (4.11) becomes positive.

The condition (3.12) can, in absence of the stress intensity factor  $K_{II}$ , be rewritten in an equivalent form as

$$K_I^2 = 2\gamma E_0 \quad (4.12)$$

where  $\gamma$  is the specific surface energy resisting crack growth and  $E_0$  is the initial Young's modulus. Using the expression (4.7) the Griffith condition (4.12) can be cast into a new and more convenient form

$$\frac{1}{2}(\sigma_2'')^2 - \frac{\gamma E_0}{\pi L} = 0 \quad (4.13)$$

In general,  $\gamma$  is constant only in the case of perfectly homogeneous isotropic elastic materials in pure plane strain. In the presence of plastic strain, material inhomogeneity and three-dimensional stress fields, the resistance to crack growth is not constant as demonstrated by so called R-curves measured in metal fracture experiments.

It has been postulated in the past that the concept of damage surface, reminiscent of the yield surface in plasticity, could be used to model the inelastic response of rock-like materials. Recently, it was shown by Krajcinovic, et al. (1991) that a damage potential can be actually derived from rigorous energy considerations within the framework micro-to-macro transition. More specifically, it was shown by Krajcinovic, et al. (1991) that a macro-damage potential can be derived from the micro-damage potentials if the thermodynamic force on a given crack weakly depends on the exact position of all other cracks. Damage surface is viewed in this context as a piecewise smooth, convex surface enveloping all points in the space of thermodynamic forces that can be reached without change in the recorded history (microstructural rearrangements). In other words, the damage surface separates the purely elastic states (characterized by dormant preexisting microcracks) from the states in which microcracks become active (grow). Geometrically, the damage surface is the inner envelope of all planes representing the conditions under which a particular microcrack starts growing. On the microscale, the thermodynamic force was identified as a properly averaged excess in the elastic energy release rate, while the flux (change of internal variable) was identified as an increment of the Budiansky-O'Connell (1976) damage variable. On the macroscale, the inelastic change of the macrocompliance  $S^*$  was selected by Krajcinovic, et al. (1991) as a flux. As a consequence, the conjugated thermodynamic force  $Q$  must be defined as

$$Q = (1/2)(\sigma \otimes \sigma) = (1/2)\{\sigma_{11}^2, \sigma_{22}^2, \sigma_{12}^2, \dots\} \quad (4.14)$$

From (4.14) it follows that, unlike the yield surface which is defined in stress space, the damage surface has to be formulated in the space of the stress components squared. This could have been anticipated since the elastic energy release rate is a homogeneous, quadratic function of the components of the stress tensor  $\sigma$ . Krajcinovic, et al. (1991) also derived precise conditions under which a damage potential exists. The existence of the damage surface was confirmed experimentally using acoustic emission tests to measure the so-called Kaiser effect (Holcomb and Costin, 1986).

For the proposed model (Fig.4.1c), the left-hand side of the crack activation condition (4.13) satisfies the following requirements imposed on the damage potential  $\Omega$ :

- $\Omega = 0$  separates elastic states from damaged states,
- $\Omega$  is a scalar valued function of properly defined thermodynamic force  $Q = (1/2)\{\sigma_2''\sigma_2''\}$ ,
- Specific dissipation rate  $\dot{D} = Q_j \dot{q}_j = (1/2)S_{22}(\sigma_2'')^2$  constitutes a potential from which the thermodynamic forces  $Q_j$  are obtained by differentiation with respect to the flux components  $\dot{q}_j$  (representing changes in the compliance).

The damage condition (4.13) can be rewritten in the following form

$$\Omega(Q, H) = Q_2 - \bar{Q}_0(H) = 0 \quad (4.15)$$

where,  $\bar{Q}_0(H)$  is a hardening function defining the threshold magnitude of the thermodynamic force at which cracking will commence. This threshold value depends on the already accumulated history and is, therefore, path dependent. The form of the hardening function  $\bar{Q}_0(H)$  can be either determined from micromechanical considerations (as in (4.13)), postulated a priori or discerned from experimental observations (see Holcomb and Costin, 1986). Exact micromechanical analysis is possible only for a handful of cases characterized by simple and idealized crack geometries for which the expressions for the stress intensity factor  $K_I$  are available. Since the microcracks in a typical low-porosity rock specimen are irregular in shape and randomly oriented a rigorous micromechanical approach to derive  $\bar{Q}_0(H)$  does not seem to be possible. Instead, a specific form for the hardening function will be assumed based on the following reasoning. Theoretically, once a Griffith crack in a homogeneous tensile field becomes critical its further growth cannot be arrested in a homogeneous elastic material. However, in the case of real materials and short cracks the assumption of material homogeneity is not a realistic one. The internal energy barriers (such as grain boundaries, and other inhomogeneities) may and often do arrest a sufficiently short crack. As a crack grows, it propagates along the path of minimum value of the excess driving force  $(G - 2\gamma)$  overcoming a sequence of successively higher energy barriers  $\gamma(x)$  randomly distributed in its path. Consequently,  $\bar{Q}_0(H)$  must be a monotonically increasing function of the stresses (similar to the R-curve) satisfying the following conditions

$$\bar{Q}_0(q=0) = Q'_{oc} = \frac{1}{2} (\sigma'_{oc})^2 \quad \left. \frac{d\bar{Q}_0}{dq} \right|_{q=q_c} = 0 \quad (4.16)$$

where  $\sigma'_{oc}$  is the stress level at the onset of kinking. The second of conditions (4.16) reflects the localization of damage (coalescence of neighboring microcracks into one macrocrack) that is assumed to occur at the apex of the stress-strain curve (representing the ultimate strength). The kinking initiation stress  $\sigma'_{oc}$ , below the brittle-to-ductile transition, can be computed from the condition  $K_I = K_{IC}$  for  $L = 0$ , with  $K_I$  given by (3.16) and  $\tau_{eff}$  by (4.10). After simple rearrangements it follows that

$$\sigma'_{oc} = 2 \frac{K_{IC} \sqrt{\pi/(2c)} \sqrt{L^*/c} + \tau_c(u)}{1 - \mu} \quad (4.17)$$

Using the conditions (4.16), it is at the same time assumed that the position of the damage surface is determined by

$$\bar{Q}_o(H) = Q'_{oc} + \frac{Q_{uc} - Q'_{oc}}{q_{uc}^2} (2q_{uc} - q_2)q_2 \quad (4.18)$$

In (4.18) the following notation is used:

$$Q'_{oc} = (1/2)(\sigma'_{oc})^2 \quad Q_{uc} = (1/2)(\sigma''_{uc})^2 = (1/2)[b(L)\tau_{eff}(\sigma_{uc}) - \sigma_2]^2 \quad (4.19)$$

where the subscript "uc" refers to the apex of the loading segment of the  $\sigma$ - $\epsilon$  curve,  $\tau_{eff}$  is given by (4.10), and  $q_{uc}$  denotes the inelastic part of the lateral compliance (at the apex) related to the wing crack growth. It should be emphasized that the particular form of (4.18) was assumed primarily for illustration purposes and could be changed if and when test data related to the actual shape of the damage surface become available.

The flux  $\dot{q}_2$  can now be derived from the damage potential (4.15) and (4.18) using the normality property. Detailed derivation will be presented subsequently for an illustrative example in Section 5.0. Graphical interpretation of the normality rule using the damage potential (4.15) is depicted in Fig. 4.2. Once the compliance vector  $q$  is determined it is straightforward to compute the corresponding macrostrains, using expressions

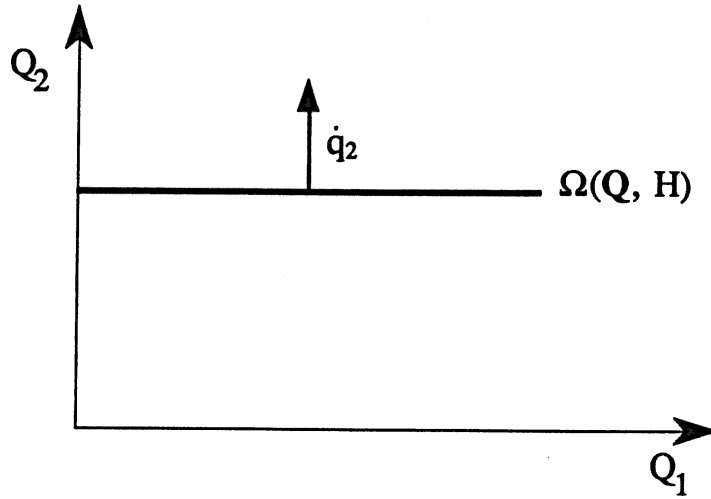


Fig 4.2. Suggested damage surface and normality rule in compression.

$$\epsilon_2^c = q_2 \sigma_2, \quad \epsilon_1^c = 0. \quad (4.20)$$

In the micromechanical analysis of strain (Section 3.0) the sliding on the preexisting flaw and the wing cracking were coupled through the expression (3.20) for the average slip. The phenomenological analysis in this section is based on the formulation of the damage potential incorporating the expression for the stress intensity factor (3.16) for a kinked crack. This expression, in a somewhat simplified but sufficiently accurate form, accounts for the above mentioned coupling between the frictional sliding on the preexisting flaw and growth of wing cracks. The total inelastic strain is obtained by summing the macrostrain attributable to frictional slip given by (4.5) and the macrostrain (4.20) due to microcracking. The strain due to initial compaction of voids  $\epsilon^v$  is not considered by the present model. An appropriate modification of the existing model in order to include the pore compaction seems to be possible without major changes. For example, using the self-consistent method it is possible to estimate the effective elastic constants of a solid with uniformly distributed spherical voids as a function of porosity. Furthermore, knowing the change of porosity as a function of stresses it becomes possible to determine the evolution equation for the change in the elastic parameters as the void density parameter is decreased.

## 5.0 ILLUSTRATIVE EXAMPLE

In this section the developed model will be applied to duplicate available experimental data for *Westerly granite* (Zoback and Byerlee, 1975) in the uniaxial compression test ( $\sigma_1 = \sigma$ ,  $\sigma_2 = 0$ ).

The following material constants were used in computations:

- elastic modulus  $E_0 = 56,500$  MPa
- Poisson's ratio  $\nu_0 = 0.25$
- coefficient of friction  $\mu = 0.5$
- compressive strength  $\sigma_{uc} = 204$  MPa
- initial cohesive shear strength  $\tau_c^0 = 24$  MPa
- fracture toughness  $K_{IC} = 1.0$  MPa $\sqrt{m}$
- initial average length of preexisting flaw  $c = 5 \cdot 10^{-4}m$
- 'initial density parameter' of preexisting cracks estimated as  $f = Nc^2 = 0.1$
- ultimate lateral strain  $\epsilon_{uc} = 0.00142$ .

At the beginning, it was necessary to compute the limits  $\sigma_{oc}$  and  $\sigma'_{oc}$  separating the elastic response, and the Phase I and Phase II responses. Since the initial closure (compaction) of preexisting cracks was not accounted for in the present model, the computed axial  $\sigma$ - $\epsilon$  curve was shifted from the origin 0 by the strain obtained from the intercept of the linear portion of the experimental curve with the  $\epsilon$ -axis. From (4.6) it follows that

$$\sigma_{oc} = \frac{2\tau_c^0}{1 - \mu} = 96 \text{ MPa} \quad (5.1)$$

Computation of  $\sigma'_{oc}$  from the expression (4.17) is not as straightforward. A rigorous analysis requires a rational, experimentally-based estimate of the degradation of the cohesive resistance  $\tau_c$  with increasing slip  $u$ . It is reported in the literature (e.g. Moss and Gupta, 1982, Nemat-Nasser and Obata, 1988) that  $\tau_c$  decays and eventually disappears as the slip on the preexisting crack accumulates. In the absence of a commonly accepted relationship based on experience if not experimental evidence, it is postulated at this point, as a simplest solution, that  $\tau_c(c)$  is a linearly decaying function of the slip strain  $\epsilon^f$

$$\tau_c = \tau_c^0 [1 - (\epsilon^f/\epsilon^s)] \quad (5.2)$$

where  $\epsilon^s$  is a scaling parameter assumed to be  $\epsilon^s = 5 \cdot 10^{-5}$ , and  $\epsilon^f$  is the strain due to sliding determined from (4.5). The constant  $\epsilon_{uc}^f$  appearing in (4.5) denotes the ultimate strain due to sliding and can be computed from the micromechanical relation (3.11). In uniaxial compression the expression for slip (3.20) reduces to

$$u = 2c \frac{1-\nu_0}{G_0} \sqrt{2 \frac{(L/c) + (L^{**}/c)}{(L/c) + (L^*/c)}} \tau_{eff} \quad (5.3)$$

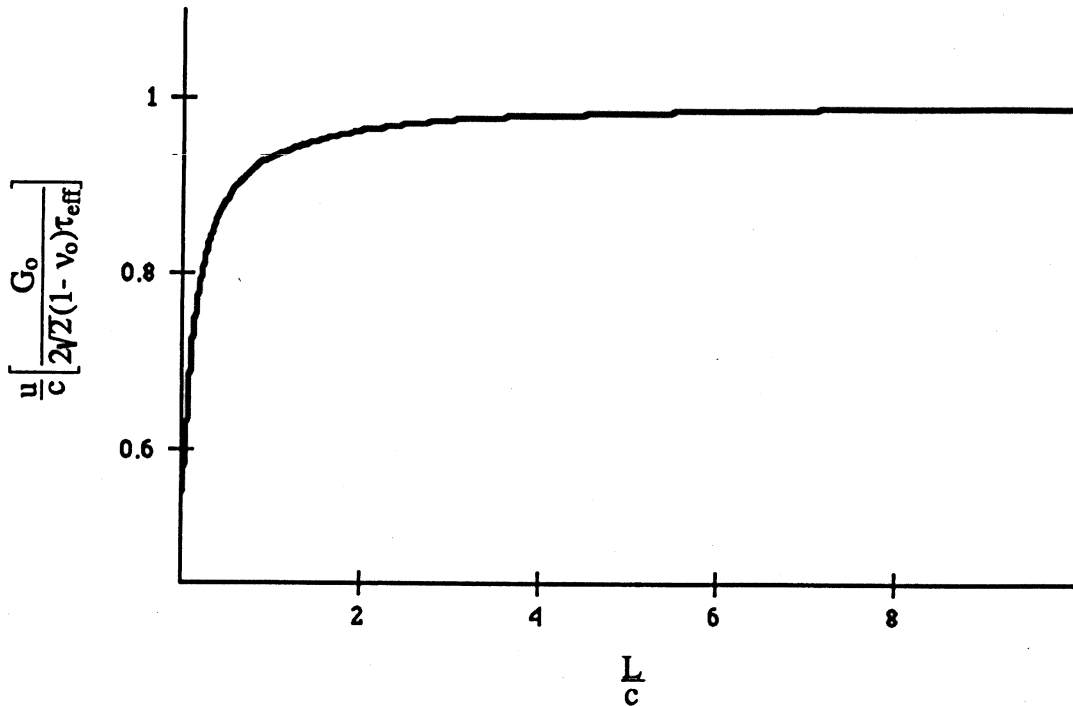


Fig. 5.1. Slip vs. wing length relationship in uniaxial compression computed from (5.3).

The nondimensionalized slip-displacement vs wing-length curve based on the expression (5.3) is plotted in Fig.5.1. The plotted curve indicates that during the advanced stage of the wing growth,  $L/c > 1$  (Fig.3.3), the slip does not depend on  $L$ . Consequently, the expression (5.3) can be further simplified to

$$u = 2c \frac{1-\nu_o}{G_o} \sqrt{2} \tau_{\text{eff}} = c \sqrt{2} \frac{1-\nu_o}{G_o} (1-\mu) \sigma \quad (5.4)$$

In (5.4) it is tacitly assumed that the cohesive strength  $\tau_c$  vanishes at the apex of the  $\sigma$ - $\epsilon$  curve. Inserting (5.4) into the formula (3.11) and setting  $\sigma = \sigma_{uc}$  it follows that

$$\epsilon_{uc}^f = 2\sqrt{2} f \frac{1-\nu_o^2}{E_o} (1-\mu) \sigma_{uc} \quad (5.5)$$

From (4.17), (4.5), (5.2) and (5.5) it finally follows that

$$(\sigma'_{oc})^2 (B \epsilon_{uc}^f) + \sigma'_{oc} [(\sigma_{uc} - \sigma_{oc})^2 - 2\sigma_{oc} B \epsilon_{uc}^f] + B \epsilon_{uc}^f \sigma_{oc}^2 - A(\sigma_{uc} - \sigma_{oc})^2 = 0 \quad (5.6)$$

where:

$$A = [2K_{IC} \sqrt{\pi/(2c)(L^*/c)} + 2\tau_c^0]/(1-\mu) \quad B = 2\tau_c^0 [\epsilon_s(1-\mu)]^{-1} \quad (5.7)$$

The axial stress at the onset of kinking computed from (5.6) is found to be  $\sigma'_{oc} = 137.3$  Mpa.

The next step consists in computing the axial and lateral strains in Phase II from (4.5). In (4.5) it was arbitrarily assumed that the exponent  $n = 2$ .

The inelastic axial strain during Phase III deformation can be determined using the expression (4.5) already used for Phase II. The lateral macrostrain can subsequently be computed from (4.20). Substituting (4.18) into (4.15) and rearranging the ensuing relation it follows that

$$q_2 = q_{uc} \left( 1 - \sqrt{\frac{\sigma_{uc}^2 - \sigma^2}{\sigma_{uc}^2 - \sigma_{oc}^2}} \right) \quad (5.8)$$

where

$$q_{uc} = \frac{2}{b(1-\mu)} \frac{\epsilon_{uc} - (\nu_o \sigma_{uc} E_o^{-1} + \epsilon_{uc}^f)}{\sigma_{uc}} \quad (5.9)$$



In (5.9) the crack aspect ratio  $b(L)$  denotes the parameter defined by (4.9). Obviously, the parameter  $b$  changes with wing crack growth. However, in order to keep the analysis as simple as possible, an average value of  $b(L = 2c) = 0.214$  was adopted for this calculation.

The final graph of stress vs. axial and lateral strain is presented in Fig. 5.2. The excellent agreement with the experimental data is not entirely surprising since some of the material constants ( $\epsilon_{uc}$ ,  $\sigma_{uc}$ ,  $n$ ,  $f$ ,  $\epsilon_s$ ) were fitted from these experimental curves. However, several important features of the brittle response of granite are indeed predicted by this simple model. For instance, the overall trend is preserved for both curves and the lateral inelastic strain is larger than its axial counterpart. It is also notable that precise and realistic numerical values were selected for all other material constants listed at the beginning of this section of the report. It is anticipated that, if lateral confinement were present, the simple "hardening" function (4.17), defining the R-curve effect, would have to be modified once actual experimental data became available. A phenomenological model based on the instability of a single crack will not be able to predict a cooperative type of final failure typical of the confined rock specimen. In such a case the microcrack interaction is a dominating mechanism in formation of a crack band and must be, as such, properly accounted for in future modeling efforts.

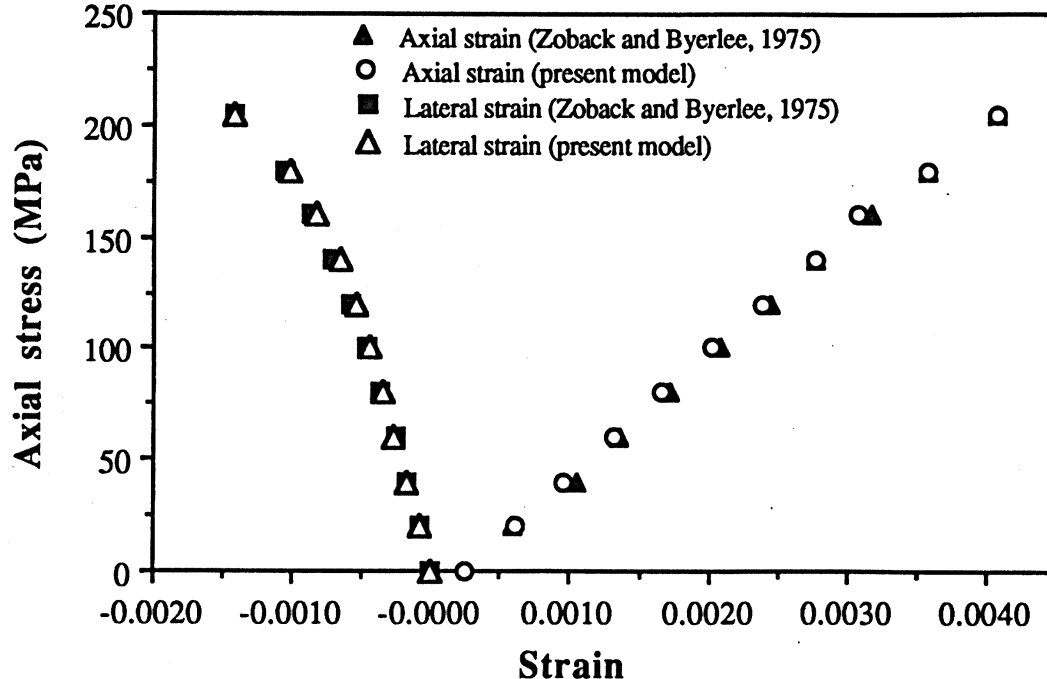


Fig 5.2 Stress-strain curve for uniaxial compression of a Westerly granite specimen.

## 6.0 REMARKS ON THE BRITTLE-TO-DUCTILE TRANSITION

Another outstanding feature yet to be analyzed and incorporated into this model is the brittle-to-ductile transition observed in rock deformation processes. The brittle-to-ductile transition point is that ratio of the lateral (confining) to axial stress beyond which failure is preceded by substantial inelastic deformation. The lateral (confining) pressure suppresses the unstable growth of the wing cracks leading to the appearance of plastic zones around the tips of the preexisting cracks AA', Fig. 3.3. Analytical description of the transition from brittle to ductile behavior of a rock is a complex problem involving studies of the relative contributions of energies dissipated in brittle and ductile modes. For example, Horii and Nemat-Nasser (1986) suggested that the appropriate parameter defining the transition is the ductility ratio

$$\Delta = \frac{K_{IC}}{\tau_Y \sqrt{\pi c}} \quad (6.1)$$

In (6.1)  $K_{IC}$  is the fracture toughness (critical stress intensity factor), and  $\tau_Y$  is the yield stress for a considered rock. "Exact" micromechanical analyses of the brittle-to-ductile transition presented in Horii and Nemat-Nasser (1986) are very complicated and involve the numerical solution of integral equations. For this reason their approach may not be entirely useful as a part of a phenomenological model suitable for applications. However, for low-porosity rocks like granite, applications of (6.1) may be quite practical. The ductility ratio (6.1) for Westerly granite was found to be  $\Delta \approx 0.05$ . According to the graphs in Horii and Nemat-Nasser (1986) this value of  $\Delta$  indicates that the transition from the brittle mode of deformation to the ductile mode occurs without entering the so-called transition mode in which the brittle and ductile effects are coupled. Thus, brittle and ductile response can be considered separately, completely ignoring the interaction effects. Naturally, experimental evidence and corroboration of these results would be necessary prior to making definitive statements.

The present report is focused solely on a model for the brittle response. The extension of the model to incorporate ductile response may require considerations of the concept of a Dugdale crack (Kanninen and Popelar, 1985). In order to determine the strains resulting from plastic deformation around the crack tips it would be necessary to compute the size of the plastic zone  $L_p$ . Preliminary computations indicate that the magnitude of  $L_p$  can be obtained in an analytical form.

## 7.0 SUMMARY AND CONCLUSIONS

The analytical model discussed in this report presents, in essence, a feasibility study needed to ascertain the effort required to formulate a micromechanically inspired constitutive model for characterizing rocks in in-situ conditions. The ultimate objective of this research program is to improve the constitutive laws used as input for the specialized computer software for analyses of shock and cratering problems. Consequently, simplicity of formulation is considered to be a vital condition for this stage of the research. Moreover, in view of a parallel effort on the experimental identification of material constants and trends in deformation it is mandatory to ensure clear and unambiguous identification of all constituent parameters of the analytical model.

Based on the work completed herein, supporting work available in published literature and previously completed studies by the authors of this report, we conclude that a reasonably simple, micromechanically inspired phenomenological constitutive model can indeed be formulated within a reasonably limited period of time. For simple, proportional loading conditions such a model will assume a rather simple form. However, in the case of arbitrary nonproportional and/or cyclic loading conditions the analytical model will become increasingly more complex. Moreover, analogous problems are typically encountered in analyses of ductile deformations. Hence, in combining brittle and ductile deformation modes the level of complexity will be enhanced. The unilateral constraint imposed by a crack on the displacement field seems to be the major problem source. Unlike plastic slip, the crack opening displacement in an essential manner depends on the sign of the normal stress. Thus, analyses considering loading paths characterized by change of normal stresses from tensile to compressive and vice versa, will by their very nature involve discontinuous changes of material stiffnesses. The ensuing complexities in large scale computations may reach substantial levels.

The main thrust of the research summarized in this report was directed towards the determination of dominant mechanisms of irreversible changes in microstructure of low-porosity rocks. For at least one of these mechanisms (kinked crack in elastic medium) the fundamental relations between the kinematic variables (strains and displacements) and corresponding stresses on the microscale are discussed in detail in this report. Assuming that the selected mechanism captured the main aspects of the physics of the deformation process a sequence of simplifying assumptions were introduced to enhance the tractability of the proposed model. In departure from rigorous micromechanical models, the proposed model considers only a single representative crack. Additional effort was devoted to the development of a rational scheme for the transition from

the micro to the macroscale, i.e. to describe the macrodeformations attributed to the presence and growth of the representative microdefect.

The very limited effort described in this report left few aspects of the model still unfinished and possibly not fully appreciated. For example, the selection of material parameters within this study was not based on a complete set of experimental data. Furthermore, a proper selection of material parameters such as those defining evolution of the damage surface (onset of kinking, apex of the stress-strain curve, etc.) as a function of the recorded history should eventually become better clarified. A well designed, comprehensive experimental effort is essential in this respect. A feedback loop connecting the three basic research groups (analytical, numerical and experimental) is absolutely essential to facilitate this effort and avoid costly mistakes and misunderstandings.

For example, some aspects of the overall deformation process, most notably a proper characterization of the softening regime, were barely mentioned in this report. In addition, the brittle-to-ductile transition must be fully and thoroughly investigated in order to be able to construct an appropriate analytical model. Moreover, in order to reconcile analytical predictions and experimental data the often neglected problem of size effect must be addressed from the micromechanical viewpoint. Finally, the question of associative vs. nonassociative flow rule must be resolved within the framework of a two potential function theory advocated in this report.

The kinked crack mechanism is commonly regarded as suitable for compact, low-porosity, crystalline rocks. Models emphasizing cracks emanating from compressed spherical voids (pores) may be much more suitable for less-compact sedimentary rocks of inferior strength. Thus, other mechanisms must be given appropriate attention in order to establish a reasonably general analytical tool for consideration of rock deformation.

Despite all of the limitations listed, and possibly some others, the research effort summarized here clearly indicates the power of micromechanical modeling. Thus, a claim can be made that the proposed modeling technique represents a promising avenue for the characterization of brittle rock failure.

## 8.0 REFERENCES

- Brace, W. F. and Bombolakis, E. G., 1963, "A Note on Brittle Crack Growth in Compression", *Journal of Geophysical Research*, **68**, 3709.
- Budiansky, B. and O'Connell, R. J., 1976, "Elastic Moduli of a Cracked Solid", *International Journal of Solids and Structures*, **12**, 81.
- Cotterell, B. and Rice, J. R., 1980, "Slightly Curved or Kinked Cracks", *International Journal of Fracture*, **16**, 155.
- Fanella, D. and Krajcinovic, D., 1988, "A Micromechanical Model for Concrete in Compression", *Engineering Fracture Mechanics*, **29**, 49.
- Holcomb, D. J. and Costin, L. S., 1986, "Detecting Damage Surfaces in Brittle Materials Using Acoustic Emissions", *Journal of Applied Mechanics*, **53**, 536.
- Horii, H. and Nemat-Nasser, S., 1986, "Brittle Failure in Compression: Splitting, Faulting, and Brittle-Ductile Transition", *Philosophical Transactions, Royal Society London*, **319**, 337.
- Jaeger, J. C. and Cook, N. G. W., 1979, *Fundamentals of Rock Mechanics*, 3rd Edition, Chapman and Hall, London.
- Kachanov, M., 1982, "A Microcrack Model of Rock Inelasticity, Part II: Propagation of Microcracks", *Mech of Materials*, **1**, 29.
- Kanninen, M.F. and Popelar, C.H. 1985, *Advanced Fracture Mechanics*, Oxford University Press, New York, NY.
- Kemeny, J. M. and Cook, N. G. W., 1991, "Micromechanics of Deformation in Rocks", in *Toughening Mechanisms in Quasi Brittle Materials*, 155, S. P. Shah, ed., Kluwer Acad. Publish.
- Krajcinovic, D., Basista, M. and Sumarac, D., 1991, "Micromechanically Inspired Phenomenological Damage Model", *Journal of Applied Mechanics*, **58**, 305.
- Murakami, Y., 1987, *Stress Intensity Factors Handbook*, Vols. 1 and 2, Pergamon Press, Oxford, UK.
- Lawn, B. R. and Wilshaw, T. R., 1975, *Fracture of Brittle Solids*, Cambridge University Press, Cambridge, UK.
- Nemat-Nasser, S. and Obata, M., 1988, "A Microcrack Model of Dilatancy in Brittle Materials", *Journal of Applied Mechanics*, **55**, 24.
- Nemat-Nasser, S. and Shokooh, A., "On Finite Plastic Flows of Compressible Materials With Internal Friction", *International Journal of Solids and Structures*, **16**, 495.
- Rudnicki, J. W. and Rice, J.R., 1975, "Conditions for the Localization of Deformation in Pressure-Sensitive Dilatant Materials", *Journal of the Mechanics and Physics of Solids*, **23**, 371.

Sammis, C. G. and Ashby, M. F., 1986, "The Failure of Brittle Porous Solids Under Compressive Stress States", *Acta Metallurgica*, **34**, 511.

Steif, P. S., 1984, "Crack Extension Under Compressive Loading", *Engineering Fracture Mechanics*, **20**, 463.

Zoback, M. D. and Byerlee, J. D., 1975, "The Effect of Cyclic Differential Stress on Dilatancy in Westerly Granite Under Uniaxial and Triaxial Conditions", *Journal of Geophysical Research*, **80**, 1526.

## DISTRIBUTION LIST

### DEPARTMENT OF DEFENSE

Director  
Defense Nuclear Agency  
ATTN: DFSP (Mr. C. B. McFarland)  
SPWE (Mr. A. A. Frederickson)  
SPWE (Dr. E. L. Tremba)  
SPSD (Dr. P. E. Senseny)  
Technical Library  
6801 Telegraph Road  
Alexandria, VA 22310-3398

Director  
Defense Nuclear Agency  
New Mexico Operations Office  
ATTN: FCTP (Dr. G. Y. Baladi)  
FCTP (Dr. E. J. Rinehart)  
FCTP (Dr. Robert Reinke)  
Kirtland AFB, NM 87115-5000

Director  
Defense Advanced Research Project Agency  
ATTN: Library  
3701 N. Fairfax Drive  
Arlington, VA 22203-1714

Defense Technical Information Center  
ATTN: TC  
Cameron Station  
Alexandria, VA 22314

### DEPARTMENT OF THE ARMY

Commander  
US Army Corps of Engineers  
ATTN: CERD-L (Mr. D. C. May)  
CERD-M (Dr. D. J. Leverenz)  
CEIM-SL  
Washington, DC 20314-1000

Director  
US Army Construction Engineering Research  
Laboratory  
ATTN: Technical Library  
P.O. Box 4005  
Champaign, IL 61820-1305

### DEPARTMENT OF THE ARMY (CONTINUED)

District Engineer  
US Army Engineer District, Omaha  
ATTN: CEMRO-ED-SH (Mr. Bill Gaube)  
215 North 17th Street  
Omaha, NE 68102-4978

Director  
US Army Cold Regions Research and  
Engineering Laboratory  
ATTN: Technical Library  
72 Lyme Road  
Hanover, NH 03755-1290

### DEPARTMENT OF THE NAVY

Naval Civil Engineering Laboratory  
ATTN: Code L51 (Mr. R. J. Odello)  
Technical Library  
Port Hueneme, CA 93043-5003

Naval Facilities Engineering Command  
200 Stovall Street  
ATTN: Technical Library  
Alexandria, VA 22332

### DEPARTMENT OF THE AIR FORCE

Air Force Office of Scientific Research  
ATTN: Technical Library  
Bolling AFB, DC 20332

Phillips Laboratory  
ATTN: Technical Library  
Kirtland AFB, NM 87117-6008

Air Force Civil Engineering Support Agency  
ATTN: RACS (Mr. W. S. Strickland)  
Technical Library  
Tyndall AFB, FL 32403

### DEPARTMENT OF ENERGY

Lawrence Livermore National Laboratory  
ATTN: L-53 (Technical Library)  
P.O. Box 808  
Livermore, CA 94550-0622

DEPARTMENT OF ENERGY (CONTINUED)

Los Alamos National Laboratory  
ATTN: M/S P364 (Report Library)  
P.O. Box 1663  
Los Alamos, NM 87545

Sandia National Laboratories  
ATTN: Div 3141 (Technical Library)  
P.O. Box 5800  
Albuquerque, NM 87185

DEPARTMENT OF DEFENSE CONTRACTORS

Mr. J. L. Bratton  
Applied Research Associates, Inc.  
4300 San Mateo Blvd., NE, Suite A220  
Albuquerque, NM 87110

Dr. J. G. Trulio  
Applied Theory, Inc.  
930 S. LaBrea Avenue  
Los Angeles, CA 90036

Dr. Dusan Krajcinovic  
Mechanical and Aerospace Engineering  
Arizona State University  
Tempe, AZ 85287-6106

Dr. Y. Marvin Ito  
California Research & Technology Division  
The Titan Corporation  
20943 Devonshire Street  
Chatsworth, CA 91311-2376

Dr. Martin Ostojja-Starzewski  
Department of Metallurgy, Mechanics and  
Materials Science  
Michigan State University  
East Lansing, MI 48824-1226

New Mexico Engineering Research Institute  
ATTN: Technical Library  
University of New Mexico  
Box 25, University Station  
Albuquerque, NM 87131

Dr. Howdy Pratt  
Science Applications International  
Corporation  
10260 Campus Point Dr.  
San Diego, CA 92121

DEPARTMENT OF DEFENSE CONTRACTORS (CONT.)

Dr. K. D. Pyatt, Jr.  
S-CUBED  
A Division of Maxwell Labs, Inc.  
P.O. Box 1620  
La Jolla, CA 92038-1620

Dr. A. L. Florence  
Dr. Lynn Seaman  
Technical Library  
SRI International  
333 Ravenswood Avenue  
Menlo Park, CA 94025

Dr. C. W. Felice  
Dr. A. H. Jones  
Terra Tek, Inc.  
420 Wakara Way  
Salt Lake City, UT 84108

Mr. Norman Lipner  
TRW Defense Systems Group  
P.O. Box 1310  
San Bernardino, CA 92402

Dr. I. S. Sandler  
Weidlinger Associates  
333 Seventh Avenue  
New York, NY 10001

Dr. Jeremy Isenberg  
Weidlinger Associates  
4410 El Camino Real, Suite 110  
Los Altos, CA 94022